

Interfacial defect engineering and photocatalysis properties of hBN/MX_2 (M = Mo, W, and X = S, Se) heterostructures

Zhi-Hai Sun(孙志海), Jia-Xi Liu(刘佳溪), Ying Zhang(张颖), Zi-Yuan Li(李子源), Le-Yu Peng(彭乐宇), Peng-Ru Huang(黄鹏儒), Yong-Jin Zou(邹勇进), Fen Xu(徐芬), and Li-Xian Sun(孙立贤)

Citation: Chin. Phys. B, 2022, 31 (**6**): 067101. DOI: 10.1088/1674-1056/ac43b2
Journal homepage: http://cpb.iphy.ac.cn; http://iopscience.iop.org/cpb

What follows is a list of articles you may be interested in

Passivation and dissociation of P_b-type defects at a-SiO_2/Si interface

Xue-Hua Liu(刘雪华), Wei-Feng Xie(谢伟锋), Yang Liu(刘杨), and Xu Zuo(左旭)
Chin. Phys. B, 2021, 30 (**9**): 097101. DOI: 10.1088/1674-1056/ac0e20

Bilayer twisting as a mean to isolate connected flat bands in a kagome lattice through Wigner crystallization

Jing Wu(吴静), Yue-E Xie(谢月娥), Ming-Xing Chen(陈明星), Jia-Ren Yuan(袁加仁), Xiao-Hong Yan(颜晓红), Sheng-Bai Zhang(张绳百), and Yuan-Ping Chen(陈元平)
Chin. Phys. B, 2021, 30 (**7**): 077104. DOI: 10.1088/1674-1056/abd7d6

Passivation of PEA^+ to $MAPbI_3$ (110) surface states by first-principles calculations

Wei Hu(胡伟), Ying Tian(田颖), Hong-Tao Xue(薛红涛), Wen-Sheng Li(李文生), and Fu-Ling Tang(汤富领)
Chin. Phys. B, 2021, 30 (**4**): 047101. DOI: 10.1088/1674-1056/abccb7

A simple rule for finding Dirac cones in bilayered perovskites

Xuejiao Chen(陈雪娇), Lei Liu(刘雷), Dezhen Shen(申德振)
Chin. Phys. B, 2019, 28 (**7**): 077106. DOI: 10.1088/1674-1056/28/7/077106

Realization of low-energy type-Ⅱ Dirac fermions in $(Ir_{1-x}Pt_x)Te_2$ superconductors

Bin-Bin Fu(付彬彬), Chang-Jiang Yi(伊长江), Zhi-Jun Wang(王志俊), Meng Yang(杨萌), Bai-Qing Lv(吕佰晴), Xin Gao(高鑫), Man Li(李满), Yao-Bo Huang(黄耀波), Hong-Ming Weng(翁红明), You-Guo Shi(石友国), Tian Qian(钱天), Hong Ding(丁洪)
Chin. Phys. B, 2019, 28 (**3**): 037103. DOI: 10.1088/1674-1056/28/3/037103

Interfacial defect engineering and photocatalysis properties of hBN/MX_2 (M = Mo, W, and X = S, Se) heterostructures

Zhi-Hai Sun(孙志海), Jia-Xi Liu(刘佳溪), Ying Zhang(张颖), Zi-Yuan Li(李子源), Le-Yu Peng(彭乐宇), Peng-Ru Huang(黄鹏儒)†, Yong-Jin Zou(邹勇进), Fen Xu(徐芬), and Li-Xian Sun(孙立贤)‡

School of Material Science and Engineering, Guilin University of Electronic Technology, Guangxi Key Laboratory of Information Materials, Guangxi Collaborative Innovation Center of Structure and Property for New Energy and Materials, Guilin 541004, *China*

(Received 18 October 2021; revised manuscript received 8 December 2021; accepted manuscript online 16 December 2021)

Van der Waals (VDW) heterostructures have attracted significant research interest due to their tunable interfacial properties and potential applications in many areas such as electronics, optoelectronic, and heterocatalysis. In this work, the influences of interfacial defects on the electronic structures and photocatalytic properties of hBN/MX_2 (M = Mo, W, and X = S, Se) are studied using density functional theory calculations. The results reveal that the band alignment of hBN/MX_2 can be adjusted by introducing vacancies and atomic doping. The type-I band alignment of the host structure is maintained in the heterostructure with n-type doping in the hBN sublayer. Interestingly, the band alignment changed into the type-II heterostructrue due to V_B defect and p-type doping is introduced into the hBN sublayer. This can conduce to the separation of photo-generated electron–hole pairs at the interfaces, which is highly desired for heterostructure photocatalysis. In addition, two Z-type heterostructures including hBN(Be_B)/MoS_2, hBN(Be_B)/$MoSe_2$, and hBN(V_N)/$MoSe_2$ are achieved, showing the decreasing of band gap and ideal redox potential for water splitting. Our results reveal the possibility of engineering the interfacial and photocatalysis properties of hBN/MX_2 heterostructures via interfacial defects.

Keywords: hBN/MX_2 heterostructures, interfacial defect, electronic state, photocatalytic properties

PACS: 71.15.Mb, 73.20.At, 74.78.Fk, 78.20.Ci **DOI:** 10.1088/1674-1056/ac43b2

1. Introduction

Two-dimensional (2D) materials have attracted intensive research interest since the discovery of graphene, in which excellent photoelectric, thermoelectric, mechanical, and chemical properties have been reported, making these materials ideal candidates for new-generation nanoscale devices.[1–6] Most of the 2D materials, including hexagonal boron nitride (hBN),[7] transition metal dichalcogenides (TMDCs),[8] black phosphorus (BP),[9] layered double hydroxides (LDHs),[10] antimonene,[11] and germanene,[12] can be prepared by the methods such as mechanical exfoliation[13] and chemical vapor deposition (CVD).[14] For two decades of investigations, extensive efforts have been devoted to tailoring 2D materials to meet the desired properties for practical applications. One of the most popular strategies is to stack different 2D components together to form heterostructures of different functionalities, and has open up a new paradigm of interface engineering.[15,16]

When two 2D materials are vertically stacked together, owing to the work function differences and charge transfer, the band alignment at the interface will be modified. For instance, Deng *et al.*[17] reported that the Schottky barrier height (SBH) of graphene/g-GaN heterostructures are effectively turned by controlling the interlayer distance. Sun *et al.*[18] developed a method of tuning the electrical characteristics of graphene/WSe_2 heterostructures through changing the interlayer coupling and a perpendicular electric field. In addtion, the physicochemical properties of heterostructures can be changed when defects exist in the interface. Fang *et al.*[19] demonstrated that interfacial defects give rise to a significant influence on the electronic states of AlN/MoS_2 heterostructures, in which different types of vacancies and dopants have different effects on the band arrangement and magnetic properties modifications. Zhao *et al.*[20] found that the heptazine/triazine based g-C_3N_4 heterostructure with the (F, Ti) co-doped interface can not only improve visible light absorption, but also promote electron–hole pairs separation and inhibit carrier recombination. Xu *et al.*[21] designed a Z-type photocatalyst (hBN/g-C_3N_4) through interfacial defect-engineereing and revealed the effects of different defects on the interface of hBN/g-C_3N_4 heterostructures. All these studies highlight the important role of interfacial defect engineering in developing of efficient novel nanoscale devices.

Here in this work, We construct a heterostructure composed of MX_2 (M = Mo, W, and X = S, Se) and hBN, and investigate the influences of interfacial defects on the electronic structures and photocatalytic properties of heterostructures in detail by using density functional theory calculations. The results exhibit that interfacial defect engineering can not only change the band aligment of heterostructures but also control

†Corresponding author. E-mail: pengruhuang@guet.edu.cn
‡Corresponding author. E-mail: sunlx@guet.edu.cn

© 2022 Chinese Physical Society and IOP Publishing Ltd

the types of photocatalysts, thereby providing a detailed guidance of design the new photocatalysts.

2. Computational methods

In this work, all calculations are performed using the Vienna *ab initio* simulation package (VASP), which is based on density functional theory (DFT) in a plane-wave basis set with the projector augmented wave (PAW) method.[22–24] The exchange correlation functional is approximated by the generalized gradient approximation of Perdew, Burke, and Ernzerhof (GGA-PBE).[25] The DFT-D3 in the Grimme approach is adopted since the GGA for exchange and correlation fails to explain the interaction between the layered structures.[26] In all calculations spin-polarization is taken into account. After the convergence test, the energy cutoff for plane-wave expansion is set to be 500 eV and a K-mesh to be $11\times11\times1$ within the Brillouin zone. The energy convergence value of the Kohn–Sham equation using the self-consistent loop is set to be 1×10^{-5} eV/atom, and the maximum stress is controlled to be within 0.01 eV/Å. To avoid the interaction between adjacent periodic images, a large vacuum spacing of 20 Å is introduced. The electron configurations of the outer nucleus considered in the pseudopotential calculation are Be($2s^2$), B($2s^22p^1$), C($2s^22p^2$), N($2s^22p^3$), O($2s^22p^4$), Mg($3s^2$), Si($3s^23p^2$), S($3s^23p^4$), Se($3d^{10}4s^24p^4$), Mo($4d^55s^1$), and W($4f^{14}5d^46s^2$). The VASPKIT program is used for data post-processing.[27]

The values of binding energy (E_b) between the hBN and MX_2 (M = Mo, W, and X = S, Se) monolayers are calculated from[17]

$$E_b = [E_{BN/MX_2} - E_{BN} - E_{MX_2}]/N_{B/N}, \tag{1}$$

where E_{BN/MX_2}, E_{BN}, and E_{MX_2} are energy of the heterostructure, isolated hBN and MX_2 monolayers, respectively; and $N_{B/N}$ is the number of boron (nitrogen) atoms in the supercell. The negative value of E_b denotes a bound system, the more strongly the hBN and MX_2 monolayers are bound together, the smaller the value is.

To obtain a better understanding of interlayer interaction, the difference in charge density $\Delta\rho$ between hBN and MX_2 is calculated from

$$\Delta\rho = \rho_{BN/MX_2} - \rho_{BN} - \rho_{MX_2} \tag{2}$$

in which ρ_{BN/MX_2}, ρ_{BN}, and ρ_{MX_2} are the plane-averaged charge densities of the hBN/MX_2 heterostructure, hBN and MX_2, respectively.

The formation energy (E_f) for V_B (V_N)-hBN/MX_2, and D_B(D_N)-hBN/MX_2 are calculated from Eqs. (3) and (4), respectively, as follows:[28]

$$E_f = E_{V_B(V_N)-BN/MX_2} - E_{BN} - E_{MX_2} + \mu_{B(N)}, \tag{3}$$

$$E_f = E_{D_B(D_N)-BN/MX_2} - E_{BN} - E_{MX_2} + \mu_{B(N)} - \mu_D, \tag{4}$$

in which $E_{V_B(V_N)-BN/MX_2}$, $E_{D_B(D_N)-BN/MX_2}$, E_{BN}, and E_{MX_2} are the total energy of V_B(V_N)-hBN/MX_2, D_B(D_N)-hBN/MX_2, hBN, and MX_2, respectively. μ_B, μ_N, and μ_D are the chemical potential of B, N, and D atoms, respectively. The negative value of E_f represents exothermic reaction in the experimental synthetic process, and lower E_f implies a more stable state.

3. Results and discussion

3.1. Pristine hBN/MX_2 heterostructures

Firstly, we optimize the geometry of monolayer MoS_2, $MoSe_2$, WS_2, WSe_2, hBN, and hBN without defects. All of these 2D materials possess a hexagonal crystal structure (space group: $P6_3/mmc$) separately with the calculated lattice constant of 2.512 Å, 3.190 Å, 3.327 Å, 3.191 Å, and 3.327 Å. The calculated geometries are consistent well with the experimental values.[28] Figure 1 shows the supercell of hBN/MS_2 heterostructure composed of $5\times5\times1$ hBN and $4\times4\times1$ MS_2 (M = Mo or W) and that of hBN/MSe_2 composed of $4\times4\times1$ hBN and $3\times3\times1$ MSe_2 (M = Mo or W). The lattice mismatches of the two kind of heterostructures are 1.6% and 0.7%, respectively. The detailed geometry and binding energy of the structures can be seen in Fig. S1 in supporting information.

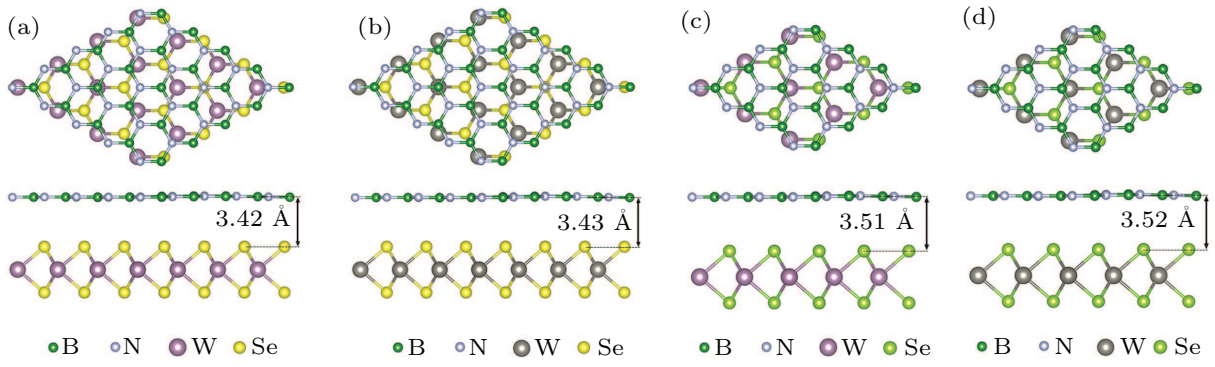


Fig. 1. Schematic illustration of crystal structures of (a) hBN/MoS_2, (b) hBN/WS_2, (c) hBN/$MoSe_2$, and (d) hBN/WSe_2.

Figure 2 shows the band structures and atomic projected densities of states (PDOSs) of the heterostructures and their components. As can be seen from the band structures, the band gap of monolayer hBN, MoS_2, WS_2, $MoSe_2$, and WSe_2 are calculated to be 4.35 eV, 1.61 eV, 1.80 eV, 1.42 eV, and 1.53 eV, respectively. As is well known, the PBE functional underestimates the band gap of hBN monolayer and MX_2 monolayer (Table 1). However, here in this work, we mainly focus on the trend of variation. Generally, the band gap and electronic states of the hBN/MX_2 heterostructure are significantly influenced by the interlayer contact. The electrons from M (M = Mo or W) atoms contribute to the valence band maximum (VBM) and the conduction band minimum (CBM) in the PDOS (Figs. 2(a)–2(d)), indicating that the band alignment of the heterostructure is of type-I. When they are stacked together, the band gap of the composed structures will be modified. For example, the band gap of the hBN/MoS_2 heterostructure is about 1.73 eV, slightly larger than that of the smaller band gap (herein MoS_2) of component. However, the trend for the hBN/$MoSe_2$ is opposite, in which the 1.38 eV band gap value is 1.38 eV, smaller than minimum band gap of components (herein $MoSe_2$).

It can be concluded that the electronic properties of the hBN/MX_2 (M = Mo, W, and X = S, Se) heterostructures are not simply a superposition of the two different materials even though the hBN and MX_2 layers are combined by van der Waals forces.

Table 1. Calculated band gap E_g (in unit eV) values of monolayer hBN, MoS_2, WS_2, $MoSe_2$, WSe_2, and the reported results for comparison.

System	Method	E_g (eV)	Reference
hBN	PBE+D3	4.35	this work
	PBE	4.37	Ref. [29]
	GW	5.54	Ref. [30]
	HSE	5.56	Ref. [29]
	EXP	5.92, 5.57	Refs. [31,32]
MoS_2	PBE+D3	1.61	this work
	PBE	1.59, 1.67, 1.8	Refs. [33–35]
	GW	2.66	Ref. [34]
	HSE	2.02, 2.25	Refs. [33,34]
	EXP	2.06	Ref. [36]
WS_2	PBE+D3	1.80	this work
	PBE	1.55, 1.81	Refs. [33,34]
	GW	2.91	Ref. [34]
	HSE	1.98, 2.32	Refs. [33,34]
	EXP	1.97	Ref. [37]
$MoSe_2$	PBE+D3	1.42	this work
	PBE	1.33, 1.44	Refs. [33,34]
	GW	2.31	Ref. [34]
	HSE	1.72, 1.99	Refs. [33,34]
	EXP	1.55	Ref. [38]
WSe_2	PBE+D3	1.53	this work, Ref. [18]
	PBE	1.25, 1.55	Refs. [33,34]
	GW	2.51	Ref. [34]
	HSE	1.63, 2.10	Refs. [33,34]
	EXP	1.65	Ref. [39]
hBN/MoS_2	PBE+D3	1.73	this work
	EXP	1.74	Ref. [40]
hBN/WS_2	PBE+D3	1.90	this work
	EXP	2.14	Ref. [41]
hBN/$MoSe_2$	PBE+D3	1.38	this work
	PBE+optB86b	1.49	Ref. [42]
hBN/WSe_2	PBE+D3	1.47	this work
	GW	2.30	Ref. [43]

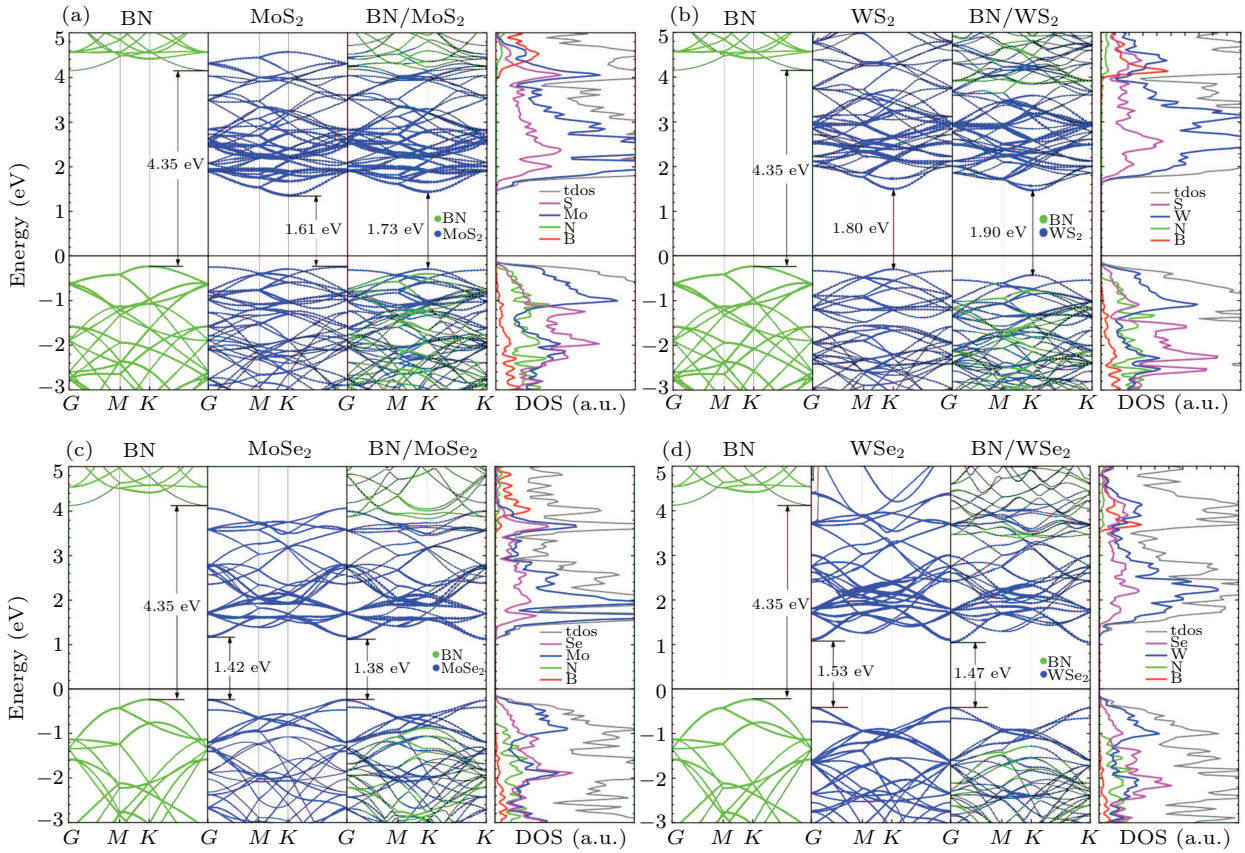


Fig. 2. Calculated energy band structures and atomic PDOSs (in arb. units) of monolayers and heterostructures: (a) hBN/MoS_2, (b) hBN/WS_2, (c) hBN/$MoSe_2$, and (d) hBN/WSe_2.

3.2. Heterostructures with vacancies in hBN

Vacancy defects usually exist in the experimental process of single-layer hBN prepared by electron beam irradiation and thermal annealing.[44,45] And vacancy defects have great effects on the excitation, migration, and recombination of photo-generated electron–hole pairs in semiconductor materials. Therefore, it is necessary to study the interface vacancy defects of heterostructures in detail. Here, the influences of B vacancy (V_B) and N vacancy (V_N), in hBN layer on the electronic structures of hBN/MX_2 (M = Mo, W, and X = S, Se) are investigated. Figure 3 shows the position of V_B and V_N, blue and red represent the removed nitrogen atoms and boron atoms, respectively.

Figure 4 shows the calculated energy band structures and atomic PDOSs of the heterostructures. The Fermi level of V_B/MX_2 remains unchanged, while the Fermi level of V_N/MX_2 shifts up to the conduction band. In addition, the energy band arrangement of V_B/MX_2 is of type-II, while that of V_N/MX_2 remains in type-I. Particularly, the degenerate energy level induced by boron vacancy is split in V_B/MX_2 heterostructures. However, the system with vacancy defect still maintains semiconductor properties though their Fermi level crosses the energy band. It can be concluded that the interface vacancy defects can introduce the defect energy level into the band structure and change the energy band arrangement.

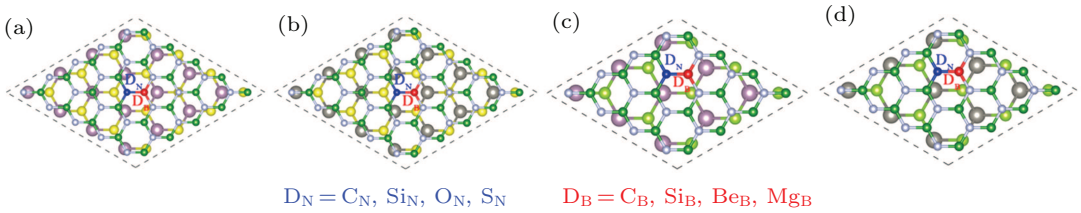


Fig. 3. Top views of doped geometrical configurations of (a) D-hBN/MoS_2, (b) D-hBN/WS_2, (c) D-hBN/$MoSe_2$, (d) D-hBN/WSe_2, with blue and red representing the atoms after having substituted for N and B atoms.

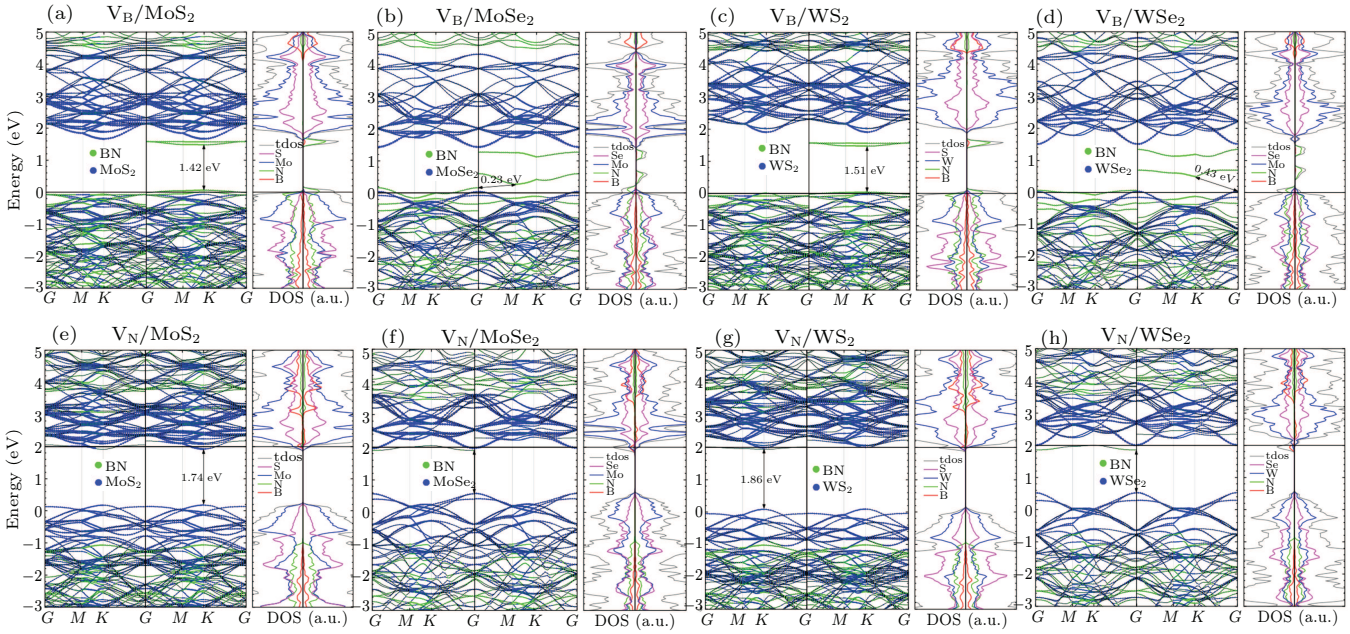


Fig. 4. Calculated energy band structures and atomic PDOSs of heterostructures: (a) V_B/MoS_2, (b) $V_B/MoSe_2$, (c) V_B/WS_2, (d) V_B/WSe_2, (e) V_N/MoS_2, (f) $V_N/MoSe_2$, (g) V_N/WS_2, and (h) V_N/WSe_2.

3.3. Heterostructures with substitutions in hBN

Doping is routinely employed to tune the electronic properties of semiconductors in many experiments.[46,47] The atoms of group (II, IV, VI)A are chosen as substitutional dopants to replace the B or N atoms of interface in hBN/MX_2. These systems are described as D-hBN/MX_2 (D = Be_B, Mg_B, C_B, Si_B, C_N, Si_N, O_N, and S_N). The top views of doped geometrical configurations are depicted in Fig. 3. To achieve n-type doping, more than one electron will be inserted into the heterostructure for each of C_B, O_N, Si_B, and S_N doping. On the other hand, C_N, Be_B, Mg_B, and Si_N are examined for the effects of p-type doping in hBN/MX_2, which a p-type doping hole is introduced into. Figure 5 shows the calculated energy band structures and atomic projected PDOSs of the atom-doped heterostructures. It can be seen that the energy band arrangement of C_B/MX_2 is of type-I, while that of C_N/MX_2 remains in type-II. The Fermi level of C_B/MX_2 shifts up to the conduction band, while the Fermi level of C_N/MX_2 keep unchanged. The carbon doped systems are greatly similar to the systems with vacancy defects. From this, it can be inferred

that V_N/V_B has n/p-type semiconductor properties. Figures S2 and S3 (in supporting information) show other types of atomic substitution systems in detail.

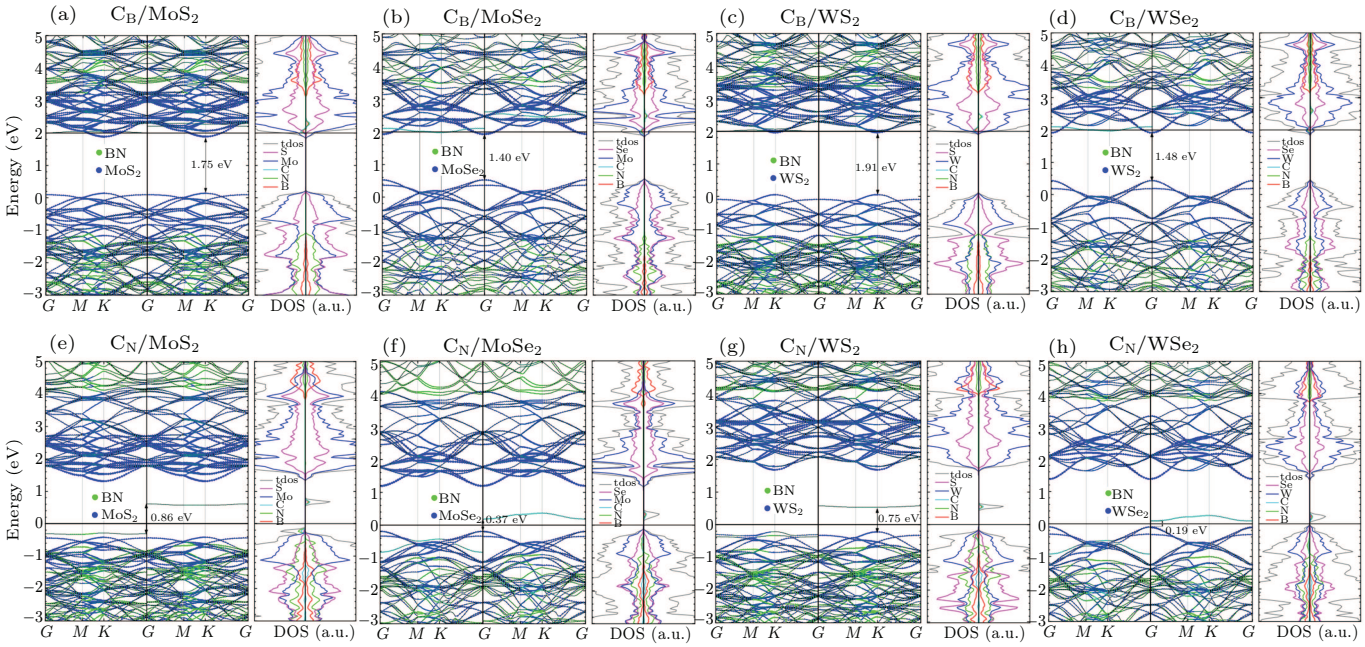


Fig. 5. Calculated energy band structures and atomic PDOSs of heterostructures: (a) C_B/MoS_2, (b) $C_B/MoSe_2$, (c) C_B/WS_2, (d) C_B/WSe_2, (e) C_N/MoS_2, (f) $C_N/MoSe_2$, (g) C_N/WS_2, and (h) C_N/WSe_2.

Figure 6(a) shows the variation of formation energy (E_f) for vacancy $V_B(V_N)$-hBN/MX_2 and for doping $D_B(V_N)$-hBN/MX_2. In the experimental synthesis process, a positive E_f value means an endothermic reaction and a negative E_f value indicates an exothermic reaction. The lower the E_f value, the more easily the reaction occurs. We find that among the four heterostructures based on MoS_2, $MoSe_2$, WS_2, and WSe_2, the hBN layer interface defect engineering is more likely to be realized on MoS_2 and WS_2 substrates. In addition, we can see that only O_N/MX_2 reaction is exothermic, while other defect types of reactions are endothermic. This can be related to the differences in atomic radius and electronegativity between impurity atoms and B(N) atoms.

For different types of substituted atoms, electronic properties of the heterostructures will change differently. Simultaneously, the work function of the host material will be modified as impurity atoms are introduced, thereby affecting the ability to bind electrons. The work function can be defined as the difference between the vacuum and the Fermi level, and calculated from[48]

$$\varphi = E_{vac} - E_F, \tag{5}$$

in which E_{vac} and E_F are the vacuum level and Fermi level, respectively. Electrons will flow from the material with the low work function through the interface to the material with the high work function, making the two different materials positively and negatively charged, respectively, resulting in an internal electric field created at the interface.

Figure 6(b) shows the work functions of D-hBN, with light blue, light magenta and light yellow regions representing the vacancy defects, n-type doping defects and p-type doping defects, respectively. Compared with intrinsic hBN, the work functions of D-hBN ($D = V_N$, C_B, Si_B, O_N, S_N, Si_N, Mg_B, and C_N) are reduced while D-hBN ($D = V_B$ and Be_B) become larger. Since the work functions of D-hBN ($D = V_N$, C_B, Si_B, O_N, S_N, and Si_N) are lower than that of the ideal MX_2, the electrons will easily flow from the D-hBN to MX_2 through the interface. This contributes to speeding up the separation of photo-generated electron–hole combination due to a built-in field that points from D-hBN ($D = V_N$, C_B, Si_B, O_N, S_N, and Si_N) to an MX_2. Moreover, the direction of electric field points from D-hBN ($D = Mg_B$ or C_N) to MX_2 in the heterostructures of Mg_B-hBN/MoS_2, C_N-hBN/MoS_2, and C_N-hBN/WS_2 while the opposite orientation of electric field exists in the heterostructures of Mg_B-hBN/WS_2, Mg_B-hBN/$MoSe_2$, Mg_B-hBN/WSe_2, C_N-hBN/$MoSe_2$, and C_N-hBN/WSe_2. We can preliminarily indicate that the MX_2 monolayer in the heterostructure D-hBN/MX_2 ($D = V_N$, C_B, Si_B, O_N, S_N, and Si_N) are acceptors of electrons and the D-hBN ($D = V_N$, C_B, Si_B, O_N, S_N, and Si_N) are donors of electrons. Conversely, the D-hBN ($D = V_B$ or Be_B) and MX_2 act as acceptor and donor of electrons in the heterostructures (V_B/MX_2, Be_B/MX_2), respectively. Figure 6(c) shows the work function of D-hBN/MX_2. With respect to the ideal hBN/MX_2, the D-hBN/MX_2 reduces the work function to some extent, which is conducive to the electrons escaping from the hBN monolayer through the interface.

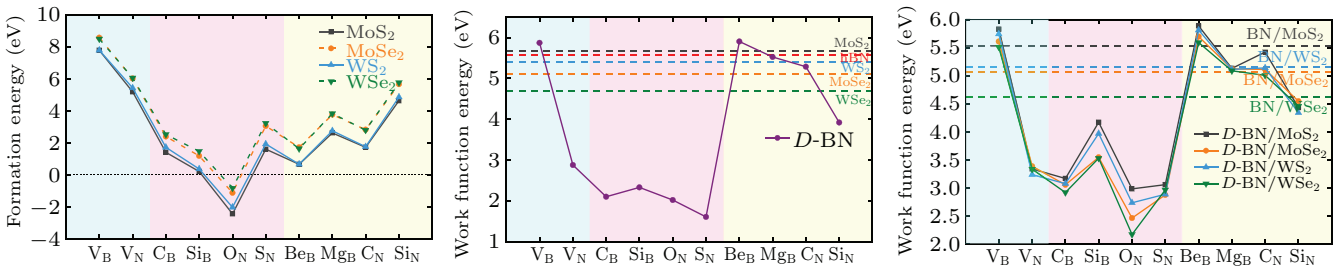


Fig. 6. (a) Total formation energy versus different vacancies and substituted atoms, (b) variation of work function with vacancy and substituted atom for (b) monolayers and (c) heterostructures, where work function of monolayers hBN, MoS_2, $MoSe_2$, WS_2, and WSe_2 are denoted by dotted red, grey, orange, blue, and olive lines, and work function of *D*-BN, *D*-hBN/MoS_2, *D*-hBN/$MoSe_2$, *D*-hBN/WS_2, and *D*-hBN/WSe_2 are represented by solid purple, grey, orange, blue, and olive curves, respectively.

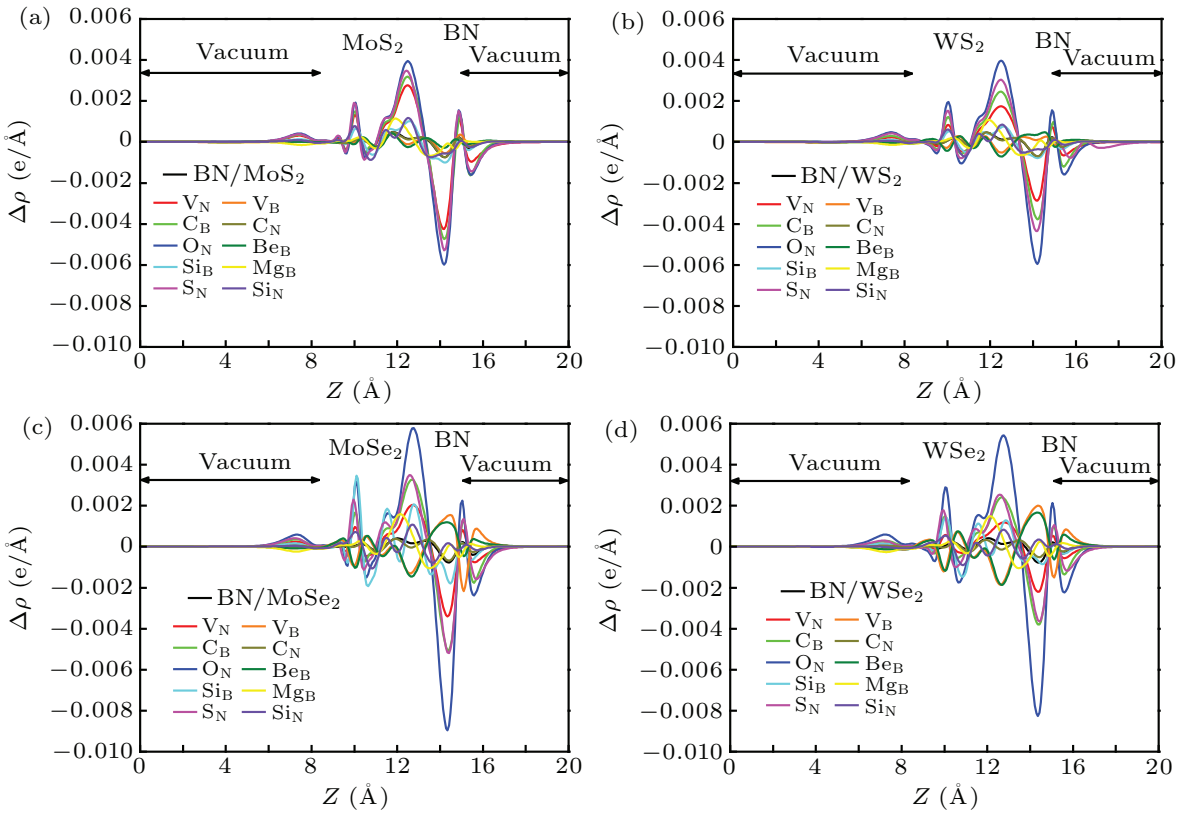


Fig. 7. Plots of plane-averaged electron density difference along the direction perpendicular to interface of (a) hBN/MoS_2, (b) hBN/$MoSe_2$, (c) hBN/WS_2, and (d) hBN/WSe_2 heterostructures under different vacancies and substituted atoms, respectively.

In order to understand the variations of the interface charge transfer and distribution with defect type and substrate materials in heterostructures, we plot the plane-averaged electron density differences along the z direction of the hBN/MX_2 heterostructures as shown in Fig. 7. Interestingly, we can find that in comparision with the ideal hBN/MX_2, the transferred charge quantity of n-type doped *D*-hBN/MX_2 ($D = C_B$, O_N, Si_B, and S_N) are significantly increased by 4 to 12 times. Especially in O_N/$MoSe_2$, the transfered charge quantity is the highest (1.5×10^{-2} e), which is much higher than intrinsic hBN/MX_2 (1.4×10^{-3} e), indicating that the interface interaction in O_N/$MoSe_2$ is the strongest. In general, the larger the transferred charge quantity, the more conducive to the separation of photo-generated electron–hole pairs it is. It can be seen from Figs. 7(c) and 7(d) that the interface electrons of *D*-hBN/MSe_2 ($D = V_B$ or Be_B) are depleted on the upper of $MoSe_2$ or WSe_2 layer, while accumulate in hBN at the lower surface, thereby generating an electric field directing from the *D*-hBN ($D = V_B$ or Be_B) to MSe_2. Accordingly, the significant interfacial interaction makes the defect degeneracy level split in V_B/MSe_2 electronic band structure. Furthermore, the induced shift in the electrostatic potential caused by the interface creation is depicted in Fig. S4, convincingly demonstrating the charge transfer direction.

As is well known, in order to improve the photocatalytic activity, not only photo-generated electron–hole pairs are required to efficiently be generated, separated and transmitted, but also the occurrence of reverse reaction must be inhibited. These are closely related to the band gap value and band arrangement of heterogeneous composite photocatalysts. The

band arrangement relative to the vacuum level can be achieved by calculating the band edge potentials of conduction band (CB) and valence band (VB) from the following formulae:[48]

$$E_{\mathrm{CB}}^{\mathrm{Vac}} = -E_{\mathrm{e}} - E_{\mathrm{CB}}^{\mathrm{NHE}} = -4.5 - (\chi - 4.5 - 0.5E_{\mathrm{g}}) = -\chi + 0.5E_{\mathrm{g}}, \quad (6)$$

$$E_{\mathrm{VB}}^{\mathrm{Vac}} = -E_{\mathrm{e}} - E_{\mathrm{VB}}^{\mathrm{NHE}} = -4.5 - (E_{\mathrm{CB}}^{\mathrm{NHE}} + E_{\mathrm{g}}) = -\chi - 0.5E_{\mathrm{g}}, \quad (7)$$

where $E_{\mathrm{CB}}^{\mathrm{Vac}}$, $E_{\mathrm{VB}}^{\mathrm{Vac}}$, $E_{\mathrm{CB}}^{\mathrm{NHE}}$, and $E_{\mathrm{VB}}^{\mathrm{NHE}}$ are the band edge positions of CB and VB relative to the absolute vacuum level (Vac) and the normal hydrogen electrode (NHE), respectively; E_{e} represents the energy of free electron on an NHE scale (4.5 eV); χ is the absolute electronegativity and its value is 5.60 eV for hBN nanosheet, 5.33 eV for MoS_2 nanosheet, 5.14 eV for MoS_2 nanosheet, WS_2: 5.54 eV for WS_2 nanosheet, and 5.34 eV for WSe_2 nanosheet; E_{g} is the band gap, which is 4.35 eV for hBN nanosheet, 1.61 eV for MoS_2 nanosheet, 1.42 eV for $MoSe_2$ nanosheet, 1.80 eV for WS_2 nanosheet, and 1.53 eV for WSe_2 nanosheet. The calculated $E_{\mathrm{CB}}^{\mathrm{Vac}}$ and $E_{\mathrm{VB}}^{\mathrm{Vac}}$ are, respectively, −3.43 eV and −7.78 eV for hBN nanosheet, −4.53 eV and −6.14 eV for MoS_2 nanosheet, −4.43 eV and −5.85 eV for $MoSe_2$ nanosheet, −4.64 eV and −6.44 eV for WS_2 nanosheet, and −4.58 eV and −6.11 eV for WSe_2 nanosheet.

The higher the CBM of photocatalyst (the more negative), the stronger the photoreduction capability is, while the lower the VBM (the more positive), the stronger the photooxidation capability is. As shown in Fig. 8, the potential at the CB edge position of *D*-hBN/MoS_2 ($D = C_B$, O_N, S_N, and Be_B) and *D*-hBN/$MoSe_2$ ($D = V_N$, C_B, Si_B, O_N, S_N, and Be_B) are more negative than ideal reduction potential (0 V), while the potential at the VB edge position is more positive than ideal oxidation potential (1.23 V). This indicates that *D*-hBN/MoS_2 ($D = C_B$, O_N, S_N, and Be_B) and *D*-hBN/$MoSe_2$ ($D = V_N$, C_B, Si_B, O_N, S_N, and Be_B) heterostructures can complete the redox reactions due to their suitable band edge potential.

Optical absorptivity, redox capability related to the position of conduction valence band, and effective separation of photo-generated carriers are the main reasons for the restriction on photocatalytic efficiency of traditional single semiconductor materials. But in the Z-type photocatalytic reaction system a two-photon excitation process is used to complete the oxidation reaction ($2H_2O + 4h^+ \rightarrow O_2 + 4H^+$) and the reduction reaction ($2H^+ + 2e^- \rightarrow H_2$) on different photocatalysts, respectively.[49–51] It can effectively inhibit the inverse reaction, showing significant advantages. We investigate the electronic properties of the Be_B/MoS_2, $Be_B/MoSe_2$, and $V_N/MoSe_2$ vdW heterostructure, the results are shown in Figs. 9(a)–9(c), respectively. Although the energy band of defect-engineered hBN crosses the Fermi level, Be_B/MoS_2, $Be_B/MoSe_2$, and $V_N/MoSe_2$ still maintain their semiconductor properties. Theoretically, there are three N atoms around each B atom in the hBN monolayer. When a single B atom is replaced by a Be atom, one N $2sp^2$ and one N $2p_z$ dangling bond will be left, resulting in an additional hole and making it a p-type semiconductor. In addition, removing one N atom to form V_N will induce three-B $2sp^2$ and three-B $2p_z$ electronic dangling bond in the plane and make it an n-type semiconductor.

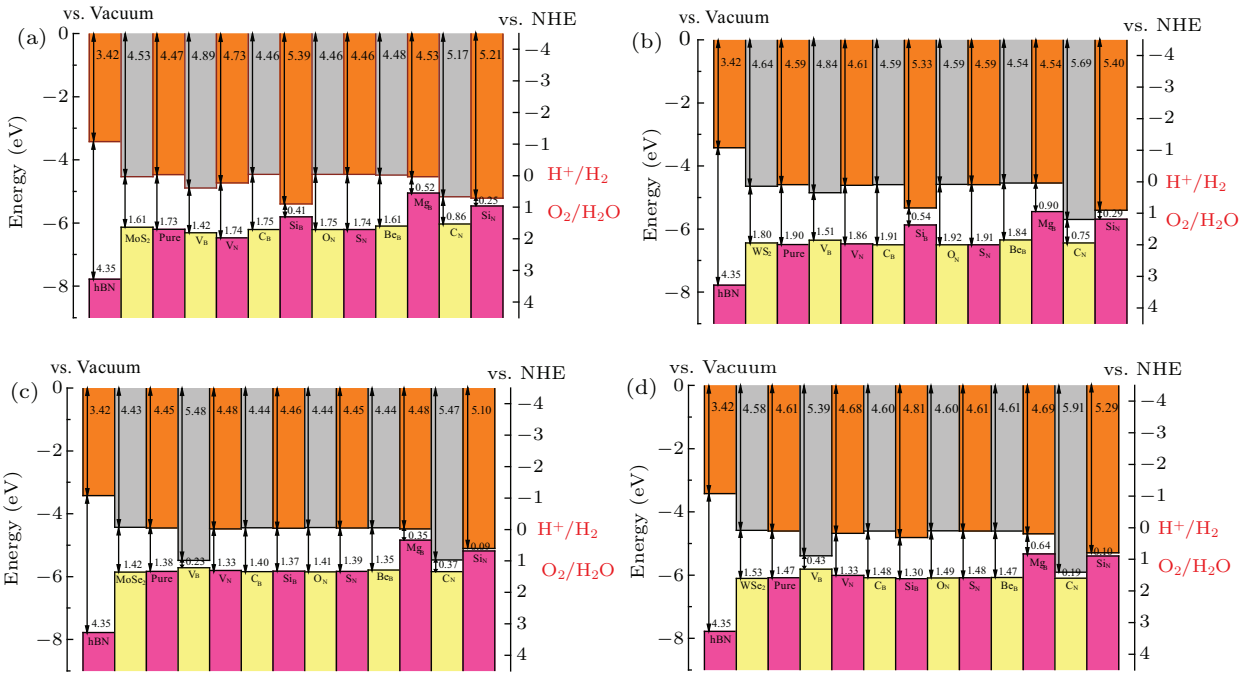


Fig. 8. Band structure diagrams of isolated hBN, MX_2 pure monolayers, and defective-engineered (a) hBN/MoS_2, (b) hBN/WS_2, (c) hBN/$MoSe_2$, and (d) hBN/WSe_2 heterostructures, relative to the redox potential for producing H_2 and O_2.

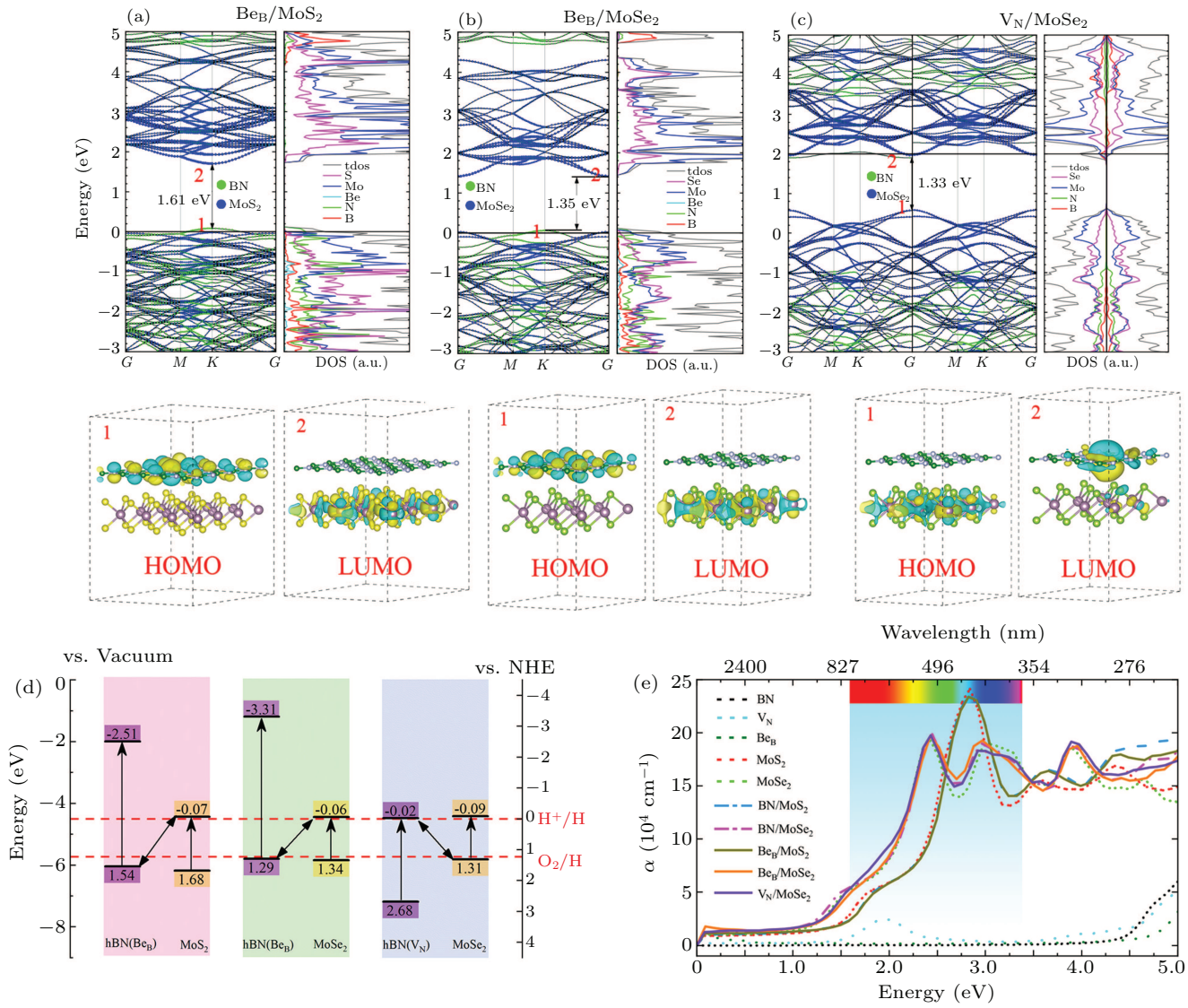


Fig. 9. Projected band structures, atomic projected PDOSs, side views of LUMO and HOMO for (a) Be_B/MoS_2, (b) $Be_B/MoSe_2$, and (c) $V_N/MoSe_2$ with an isovalue of 0.001 e/Å^3. (d) Calculated band edge potentials versus NHE for Be_B/MoS_2, $Be_B/MoSe_2$, and $V_N/MoSe_2$ at pH = 0. Their carrier transfer and separation are displayed. (e) Calculated optical absorption coefficient of isolated monolayer, perfect and defective-engineered hBN/MX_2 bilayers.

The highest occupied molecular orbital (LUMO) and the lowest unoccupied molecular orbital (HOMO) are marked with red numbers 1 and 2 in band structures as shown in Figs. 9(a)–9(c). In terms of real space, the HOMO of Be_B/MoX_2 (X = S or Se) primarily derives from the hBN layer, with P_z orbital of N atom forming π bond, while LUMO is contributed by MoX_2 (X = S or Se) layer, forming a σ bond. However, the situation of $V_N/MoSe_2$ is opposite. These can be further demonstrated through the corresponding PDOS of Be_B/MoS_2, $Be_B/MoSe_2$, and $V_N/MoSe_2$, respectively. On the one hand, the appropriate band gap is 1.61 eV for Be_B/MoS_2, 1.35 eV for $Be_B/MoSe_2$, and 1.33 eV for $V_N/MoSe_2$. On the other hand, the separation between the reduction process and oxidation process can effectively separate and transport photo-generated electron–hole pairs. Therefore, we can confirm that the Be_B/MoS_2, $Be_B/MoSe_2$, and $V_N/MoSe_2$ heterostructure form a Z-type photocatalytic reaction system.

Figure 9(d) shows two Z-type photocatalytic reactions processes with opposite photo-generated carriers transferring directions. In Be_B/MoS_2 or $Be_B/MoSe_2$, the photo-generated electrons of CB in MoX_2 (X = S or Se) with reduction reaction are prone to combining the photo-excited holes of VB in hBN(V_N) with oxidation reaction. However, the direction of carriers transferring in $V_N/MoSe_2$ is opposite to that in $Be_B/MoSe_2$. Compared with the traditional type-II heterostructure, the Z-type photocatalyst only needs to meet the requirement for its respective photoexcitation process and corresponding semi reactions, providing a tremendous space for the selection and design of photocatalytic materials. Generally, the optical absorption properties of photocatalytic semiconductor material are the macroscopic representation of its energy band structure. The calculated optical absorption coefficient of isolated monolayer, intrinsic and defect-engineered hBN/MX_2 bilayers are shown in Fig. 9(e). We can see that the defect-engineered hBN/MX_2 bilayers will effectively im-

prove the absorption coefficient of visible light and make the red shift obviously appear at the absorption boundary. In short, our results indicate that the defect-engineered interfacial heterostructures can remarkly improve the photocatalytic properties of hBN/MX_2 (M = Mo, W, and X = S, Se) by tuning band arrangement, enhancing the interface charge transfer and light response, specifically the creation of Z-type heterostructures with high redox capability.

4. Conclusions

In this paper, the effects of interfacial defects on the electronic structure, charge transfer across the interface and photocatalytic properties of hBN/MX_2 (M = Mo, W, and X = S, Se) have been systematically investigated by the first principles calculation. After introducing vacancy and element doping, the n-type doped hBN/MX_2 (M = Mo, W, and X = S, Se) heterostructures maintain the I-type band arrangement, while the p-type doping changes the band arrangement from I-type to II-type. Comparing with the ideal hBN/MX_2 (M = Mo, W, and X = S, Se), the transferred charge quantity of n-type doped D-hBN/MX_2 ($D = C_B$, O_N, Si_B, and S_N) are significantly increased by 4 to 12 times, in which the interface interaction of O_N-hBN/$MoSe_2$ is the strongest. Two Z-type photocatalytic reaction processes with opposite photogenerated carriers transferring directions are achieved by defect engineering. With the help of two-photon excitation process, the reduction process and oxidation process are separated from each other. It includes efficiently separating and transmitting photo-generated electron–hole pairs, enhancing interfacial charge transfer and light response, and improving the stability of photocatalytic system. These theoretical results are expected to provide useful guidance for designing the novel high-efficiency photocatalyst based on hBN/TMDCs heterostructure.

Acknowledgements

Project supported by the National Key Research and Development Program of China (Grant No. 2021YFB3802400), the National Natural Science Foundation of China (Grant Nos. 52161037, U20A20237, 51871065, and 51971068), the Scientific Research and Technology Development Program of Guangxi Zhuang Autonmous Region Province, China (Grant Nos. AD19110037, AA19182014, AD17195073, and AA17202030-1), the Guangxi Natural Science Foundation, China (Grant Nos. 2017JJB150085 and 2019GXNSFGA245005), the Innovation Project of GUET Graduate Education, China (Grant No. 2022YCXS197), the Guangxi Bagui Scholar Foundation, Guangxi Collaborative Innovation Centre of Structure and Property for New Energy and Materials, Guangxi Advanced Functional Materials Foundation and Application Talents Small Highlands, Chinesisch-Deutsche Kooperationsgruppe, China (Grant No. GZ1528), and the Guangxi Key Laboratory of Information Material, China (Grant No. 201025-Z).

References

[1] Novoselov K S, Geim A K, Morozov S V, Jiang D, Zhang Y, Dubonos S C, Grigorieva I V and Firsov A A 2004 *Science* **306** 666
[2] Zhang L, Yang Z, Gong T, Pan R, Wang H, Guo Z, Zhang H and Fu X 2020 *J. Mate. Chem. A* **8** 8813
[3] Cao Y, Fatemi V, Fang S, Watanabe K, Taniguchi T, Kaxiras E and Jarillo-Herrero P 2018 *Nature* **556** 43
[4] Knobloch T, Illarionov Y Y, Ducry F, Schleich C, Wachter S, Watanabe K, Taniguchi T, Mueller T, Waltl M and Lanza M 2021 *Nat. Electron.* **4** 98
[5] Chen H, Xue X, Liu C, Fang J, Wang Z, Wang J, Zhang D W, Hu W and Zhou P 2021 *Nat. Electron.* **4** 399
[6] Reserbat-Plantey A, Epstein I, Torre I, Costa A T, Gonçalves P, Mortensen N A, Polini M, Song J C, Peres N M and Koppens F H 2021 *Acs Photonics* **8** 85
[7] Shi Y, Hamsen C, Jia X, Kim K K, Reina A, Hofmann M, Hsu A L, Zhang K, Li H and Juang Z 2010 *Nano Lett.* **10** 4134
[8] Zeng Z, Yin Z, Huang X, Li H, He Q, Lu G, Boey F and Zhang H 2011 *Angew. Chem.* **123** 11289
[9] Yasaei P, Kumar B, Foroozan T, Wang C, Asadi M, Tuschel D, Indacochea J E, Klie R F and Salehi-Khojin A 2015 *Adv. Mater.* **27** 1887
[10] Wang Q and O'hare D 2012 *Chem. Rev.* **112** 4124
[11] Wang G, Pandey R and Karna S P 2015 *Acs Appl. Mater. Interfaces* **7** 11490
[12] Cahangirov S, Topsakal M, Aktürk E, Şahin H and Ciraci S 2009 *Phys. Rev. Lett.* **102** 236804
[13] Novoselov K S, Jiang D, Schedin F, Booth T, Khotkevich V, Morozov S and Geim A K 2005 *Proc. Natl. Acad. Sci. USA* **102** 10451
[14] Lee Y H, Zhang X Q, Zhang W, Chang M T, Lin C T, Chang K D, Yu Y C, Wang J T W, Chang C S, Li L J and Lin T W 2012 *Adv. Mater.* **24** 2320
[15] Wu D, Guo J, Wang C, Ren X, Chen Y, Lin P, Zeng L, Shi Z, Li X J and Shan C X 2021 *Acs Nano* **15** 10119
[16] Qi F, Yang Z, Zhang J, Wang Y, Qiu Q and Li H 2020 *ACS Appl. Mater. Interfaces* **12** 55417
[17] Deng Z, Wang X and Cui J 2019 *RSC Adv.* **9** 13418
[18] Sun M, Chou J P, Yu J and Tang W 2017 *J. Phys. Chem. C* **5** 10383
[19] Fang Q, Huang Y, Miao Y, Xu K, Li Y and Ma F 2017 *J. Phys. Chem. C* **121** 6605
[20] Zhao Y, Lin Y, Wang G, Jiang Z, Zhang R and Zhu C 2019 *Appl. Surf. Sci.* **463** 809
[21] Xu L, Zeng J, Li Q, Xia L, Luo X, Ma Z, Peng B, Xiong S, Li Z and Wang L L 2021 *Appl. Surf. Sci.* **547** 149207
[22] Kresse G and Kurthmuler J 1996 *Comput. Mater. Sci.* **6** 15
[23] Kresse G and Hafner J 1994 *Phys. Rev. B* **49** 14251
[24] Kresse G and Joubert D 1999 *Phys. Rev. B* **59** 1758
[25] Perdew J P, Burke K and Ernzerhof M 1996 *Phys. Rev. Lett.* **77** 3865
[26] Grimme S and Semiempirical 2006 *J. Comput. Chem.* **27** 1787
[27] Wang V, Xu N, Liu J C, Tang G and Geng W T 2021 *Comput. Phys. Commun.* **267** 108033
[28] Van de Walle C G and Neugebauer 2004 *J. Appl. Phys.* **95** 3851
[29] Huang B and Lee H 2012 *Phys. Rev. B* **86** 245406
[30] Biase X, Rubio A and Louie S 1994 *Europhys. Phys. Lett.* **28** 335
[31] Shi Y, Hamsen C, Jia X, Kim K K, Reina A, Hofmann M, Hsu A L, Zhang K, Li H and Juang Z Y 2010 *Nano Lett.* **10** 4134
[32] Song L, Ci L, Lu H, Sorokin P B, Jin C, Ni J, Kvashnin A G, Kvashnin D G, Lou J and Yakobson B I 2010 *Nano Lett.* **10** 3209
[33] Kang J, Tongay S, Zhou J, Li J and Wu J 2013 *Appl. Phys. Lett.* **102** 012111
[34] Ding Y, Wang Y, Ni J, Shi L, Shi S and Tang W 2011 *Physica B* **406** 2254
[35] Zhu Z Y, Cheng Y C and Schwingenschlögl U 2011 *Phys. Rev. B* **84** 153402
[36] Singh N, Jabbour G and Schwingenschlögl U 2012 *Eur. Phys. J. B.* **85** 1
[37] Albe K and Klein A 2022 *Phys. Rev. B* **66** 073413

[38] Tongay S, Zhou J, Ataca C, Lo K, Matthews T S, Li J, Grossman J C and Wu J 2012 *Nano Lett.* **12** 5576
[39] Cheng Q, Pang J, Sun D, Wang J, Zhang S, Liu F, Chen Y, Yang R, Liang N and Lu X 2020 *InfoMat* **2** 656
[40] Zhao G, Wang J, Xu Y, Ma Z, Li X, Yang W, Liu G and Yang J 2020 *J. Alloy. Compd.* **834** 155108
[41] Zhao G, Xu Y, Wang J, Li X, Yang W, Liu G and Yang J 2021 *J. Alloy. Compd.* **854** 157301
[42] Koda D S, Bechstedt F, Marques M and Teles L K 2017 *J. Electron Mater.* **46** 3910
[43] Gerber I C and Marie X 2018 arXiv:1810.02130
[44] Jin C, Lin F, Suenaga K and Iijima S 2009 *Phys. Rev. Lett.* **102** 195505
[45] Meyer J C, Chuvilin A, Algara-Siller G, Biskupek J and Kaiser U 2009 *Nano Lett.* **9** 2683
[46] Zhang J, Deng P, Deng M, Shen H, Feng Z and Li H 2020 *ACS Omega* **5** 29081
[47] Sun Z H, Huang Q, Zhang Y, Huang P R, Zhi H Y, Zou Y J, Xu F and Sun L X. 2021 *Acta Phys. Sin.* **70** 033102 (in Chinese)
[48] Wang J, Huang Y, Zhu G, Zhang J, Wei X and Ma F 2021 *J. Alloys Compd.* **859** 157873
[49] Zhang X, Wang D, Man X, Wu J, Liu Q, Qi Y, Liu Z, Zhao X, Wu J and Hao C 2020 *J. Colloid Interface Sci.* **558** 123
[50] Zhao D, Wang Y, Dong C L, Huang Y C, Chen J, Xue F, Shen S and Guo L 2021 *Nat. Energy* **6** 388
[51] Xing C, Liu Y, Zhang Y, Wang X, Guardia P, Yao L, Han X, Zhang T, Arbiol J and Soler L 2021 *ACS Appl. Mater. Interfaces* **13** 449